RESEARCH LETTER

Key Points:

- We present results from the first large-scale onshore three-component nodal geophone deployment across a subduction zone forearc
- Radial receiver function images show the major subduction zone converters including the top-of-slab, slab Moho, and continental Moho
- High-frequency receiver functions show strong continuous shallow crustal arrivals across the Siletzia terrane

High-Resolution Receiver Function Imaging Across the Cascadia Subduction Zone Using a Dense Nodal Array

K. M. Ward[1,2] (iD), F. Lin[2] (iD), and B. Schmandt[3] (iD)

[1]Department of Geology and Geological Engineering, South Dakota School of Mines and Technology, Rapid City, SD, USA, [2]Department of Geology and Geophysics, University of Utah, Salt Lake City, UT, USA, [3]Department of Earth and Planetary Sciences, University of New Mexico, Albuquerque, NM, USA

Abstract In the summer of 2017, we deployed 174 nodal geophones in the Cascadia Subduction Zone forearc with the specific aim of conducting a high-resolution receiver function study. The dense trench perpendicular line in central Oregon with 500-m spacing recorded continuous data for approximately 40 days. Our plate tectonic-scale imaging results show the same features as previous broadband seismic deployments including the top of the subducting Juan de Fuca Plate, the slab Moho, and the continental Moho. Although our deployment was limited to around 40 days, the dense station spacing allowed us to image the shallow Oregon forearc in remarkable detail. In our shallow results, we image a continuous positive arrival that we interpret as the top of the accreted Siletzia terrane. We suggest that hybrid nodal/broadband deployments could be used in conjunction with offshore seismic studies to image subduction zones in unprecedented detail.

Plain Language Summary The largest earthquakes occur along subduction zones when energy stored along the plate interface is released during great subduction zone earthquakes. A component of understanding the hazards associated with such great earthquakes is knowledge of the subsurface Earth structure. For example, understanding the plate interface geometry in detail can improve predictions of how seismic waves propagate to the surface and help inform seismic hazard maps. In this study, we explore the use of a recently available seismometer technology that enables rapid deployment of large numbers of sensors with the aim of improving knowledge of Cascadia Subduction Zone structure in central Oregon. Our findings are presented in a proof-of-concept context where we demonstrate that the new seismometer technology is capable of resolving features seen in previous studies as well as new details owing to increased seismometer density. We suggest that this deployment scheme could be scaled and leveraged with offshore seismic experiments to explore the subsurface Earth structure along an active subduction zone in unprecedented detail.

1. Introduction

From a global perspective, the Cascadia Subduction Zone is a relatively anomalous subduction zone. Its warm thermal structure (Syracuse et al., 2010) owing to the young age of the incoming plate (<10 Ma; Kirby et al., 1996) classifies it as a hot end-member subduction zone (Abers et al., 2017). Global Positioning System-derived locking models also show varying degrees of updip and downdip locking with significant along strike variability (McCaffrey et al., 2013). Furthermore, its segmented seismic nature focuses most of the Wadati-Benioff earthquakes along the northern (Washington and Vancouver Island) and southern (northern California) extremes of the margin leaving a relatively aseismic central segment (Oregon; McCrory et al., 2012). The enigmatic seismicity along this margin makes it difficult to identify spatial and temporal variations in earthquake hazards without other indirect approaches (e.g., Hyndman, 2013; Leonard et al., 2010; Wang et al., 2013).

In central Cascadia, the forearc basement in northern Oregon and southern Washington is dominated by submarine and subaerial oceanic basalts that range in age from 56 to 49 Ma (Wells et al., 2014). The irregular distribution of Siletz River Volcanics (Oregon) and the Crescent volcanic suite (Washington) represent outcrops of the larger Siletzia terrane (ST) thought to have accreted ~50 Ma. The overthickened crust of the ST is interpreted as a product of oceanic hot spot volcanism now associated with the plume that fuels the Yellowstone hot spot in the Cordilleran interior (Wells et al., 2014). Upon entering the Eocene subduction zone, the ST docked with North America deforming the edge of the Columbia Embayment and causing the
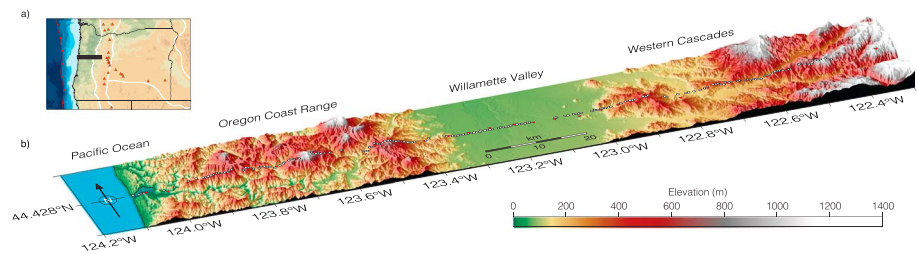
Figure 1. (a) Inset map of Oregon, USA, showing our study area (thick black line) in the Cascadia Subduction Zone tectonic context with Holocene volcanoes (red triangle), trench axis (red line), and physiographic provinces (white lines). (b) Our Cascadia 2017 nodal station location map (white circles) and older (Li & Nábělek, 1999; Nábělek et al., 1993; Tréhu et al., 1994) broadband deployment (red inverted triangles) with 3-D perspective topography. Oregon Coast Range (CR), the Willamette Valley (WV), and the Western Cascades (WC) as abbreviated in the main text.

location of the subduction zone boundary to jump ~300 km west to near its present location (Wells et al., 2014). Thus, a better understanding of the complicated upper plate structure is interesting from a tectonics standpoint but is also a key component in understanding earthquake processes at the subduction zone interface (i.e., locked portion, pore fluid pressure, and geometry).

To better understand the nature of the plate interface and the subsurface structure along a section of the Oregon forearc, and to explore the possible use of a new seismic instrument technology, we deployed 174 autonomous three-component 5-Hz Fairfield Nodal Zland geophones in central Oregon (Figure 1). The specific array design was chosen for comparison with a previous broadband seismograph deployment (Li & Nábělek, 1999; Nábělek et al., 1993; Tréhu et al., 1994). Scientific motivations for the nodal geophone deployment were twofold. First, we wanted to see if new instrument technology that afforded greater station density but shorter sampling duration could reproduce some of the radial receiver function (RF) results derived from the original broadband deployment. Second, we wanted to explore what new features could be recovered by the denser spacing of the nodal array. Here we present our new RF results and highlight future large-scale (>100 km) uses of a limited-duration but dense nodal geophone deployments.

2. Data and Methods

In the summer (June, July, and August) of 2017, the University of Utah in collaboration with the University of Arizona, the University of Oregon, and the University of New Mexico deployed 174 autonomous three-component 5-Hz Fairfield Nodal Zland geophones in central Oregon (Figure 1). The east-west (~130 km), approximately trench perpendicular line started on the coast in Waldport, Oregon, and traversed the Coast Range (CR), the Willamette Valley (WV), and the Western Cascades (WC) recording continuous data for ~40 days (battery life limit). The ~500-m station spacing represents an order of magnitude improvement on previous passive source deployments (Nábělek et al., 1993). Such high-density deployments have recently become much more practical owing to new instrument technology. Typically, these new instruments (nodes) have been used to target smaller scale (~1 km) and shallower geological features (e.g., Wu et al., 2017). Our Cascadia 2017 array (Ward & Lin, 2017) represents an early effort to utilize this technology to address lithospheric-scale imaging problems (Liu et al., 2018). Here we focus primarily on RF imaging but note that other applications are possible (e.g., surface or body wave tomography).

2.1. RFs

Individual three-component 5-Hz nodal geophones are capable of generating RFs comparable with co-located broadband seismometers (Liu et al., 2018; Ward & Lin, 2017). Although the relatively limited deployment duration of the nodes (~40 days) compared to intermediate and broadband seismometers (months to years) limits the number of teleseismic events available for RF analysis, the greater station density of the nodes allows more information to be extracted from each event. We exploit the greater station density by introducing a simple array-based approach of generating RFs that reduces noise and emphasizes true signals. This is especially useful at higher frequencies where the lateral station density allows coherent features to be distinguished from noise. Our array-based approach includes the assumption that subsurface structures are effectively laterally invariant over relatively small distances.

Individual station preprocessing of the waveform data prior to calculating radial RFs is treated the same way as outlined by Ward and Lin (2017, and references therein). Each of the nine teleseismic (30°–90°) events (>6.0 Mw) recorded by the array are windowed around the theoretical direct *P* arrival (−15:P:75 s), band-pass filtered (0.1–8.0 Hz) during the instrument removal, and rotated into the ZRT (vertical, radial, and transverse) earthquake reference frame. Our new array-based approach adds the additional step of cross correlating the vertical and radial components of each station (reference station) with every other station's equivalent component. For consistency, we shift the radial and vertical components by the same lag time measured from the maximum cross correlation of the vertical component. This allows an arbitrary distance window around the reference station to be selected (0–5 km radius in this study) where the vertical and radial components of other stations within that distance window can be moveout corrected and stacked about the reference station (Figure S1) prior to calculating RFs (Ligorría & Ammon, 1999). A distinct advantage of this additional step is the reduction of noise (particularly on horizontal components) while also providing an automated way of excluding bad stations (e.g., node was knocked over, dead channel, etc.).

After the vertical and radial traces have been moveout corrected, the correlation coefficients are calculated and only pairs with a correlation coefficient of 0.5 or greater are included in the pre-RF stack (or spatial pre-RF stack). If only one component meets these criteria, both are excluded from the stack. If the reference station is bad (e.g., correlation coefficient < 0.5), no neighboring stations are stacked from within the distance window resulting in no RF being generated for that location. We note that the correlation coefficient threshold of 0.5 or greater is arbitrary, as a threshold range from 0.15 to 0.85 would have produced the same results. This is because the correlation coefficient of bad stations is always close to 0 (<0.15), whereas the correlation coefficient of good stations is very high (>0.85).

In addition to the spatial pre-RF stacking approach afforded by the dense station spacing, temporal stacking of the RFs from multiple events (with similar back-azimuths and ray parameters) can further reduce noise and enhance robust features. Individual event RFs (i.e., no temporal post-RF stacking) are presented in Figures S2 and S4 and the associated metric of how well the deconvolution is fitting the radial components (Figures S3 and S5); however, all results shown in the main text are stacks of two events (i.e., with temporal post-RF stacking; Table S1). We also include in the supporting information a series of comparison figures (Figures S6–S8) that highlight what features are resolvable with varying station spacing along our line.

In Figure 2, we present a spatial pre-RF stacking distance window of 0 km (i.e., no spatial pre-RF stacking), 5 km (2.5 km radius), and 10 km (5 km radius); however, we note that the choice of a stacking distance window is arbitrary and have included in the supporting information an animation example (Movie S1) that cycles through stacking distance windows from 0 to 10 km in small increments (~160 m). Unfortunately, our array did not record a sufficient azimuthal distribution of useable events (high signal-to-noise ratio) to generate a common conversion point stack image (e.g., Dueker & Sheehan, 1997), suggesting that a hybrid broadband/nodal deployment strategy might provide additional imaging possibilities in the future. Nevertheless, our RF results show remarkable agreement with previous RF studies where comparable (e.g., Audet et al., 2010; Tauzin et al., 2017) while illuminating finer scale crustal structures only resolvable with the dense station spacing of our nodal array.

Typically, pushing the frequency content (Gaussian filter) of RFs to higher values (>3 Hz) is avoided because it becomes increasingly difficult to separate noise from coherent signals, except in arrays with unusually small station spacing (e.g., Leahy et al., 2012). However, dense nodal arrays allow for higher frequency RFs, and thus more detailed shallow imaging, because laterally continuous arrivals can be traced across several geophones as a qualitative discriminator (e.g., Leahy et al., 2012; Ward & Lin, 2017). Additionally, array-based approaches, such as the approach developed here, can further leverage the dense data coverage to reduce noise and enhance robust features. In Figure 3, we present an example of high-frequency RFs with a Gaussian value of 10 (~4.8 Hz) and a stacking distance window of 10 km (5-km radius). These stacked high-frequency RFs were depth-migrated using the *FuncLab Software* (Porritt & Miller, 2018) and a regional 3-D velocity model (Porritt et al., 2014).

3. Results

We focus on the primary conversions observed in our results and limit our discussion and subsequent interpretation to those features. While numerous previous studies have used the multiples (e.g., Audet et al., 2010;
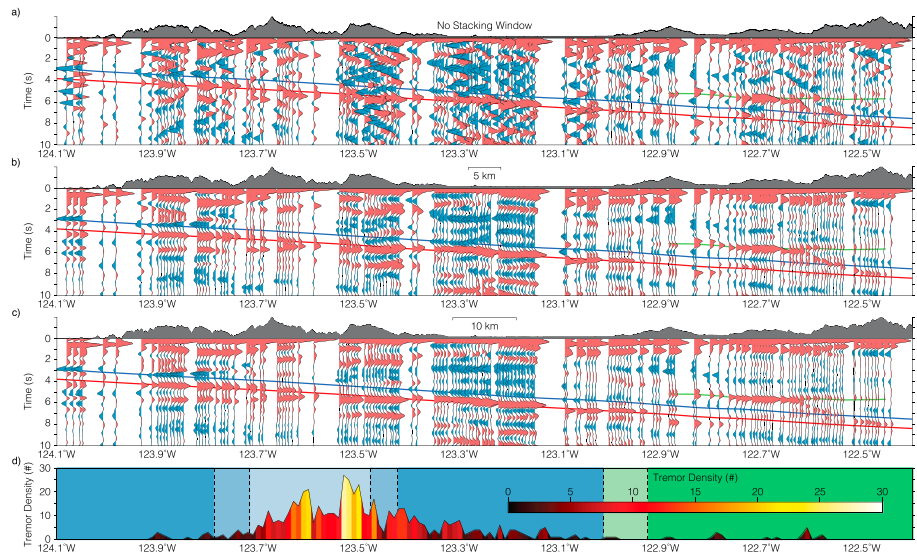
Figure 2. (a–c) Stacked radial receiver functions with a Gaussian value of 5 (~2.4 Hz) for a stacking distance window of 0 km (i.e., no stacking), 5 km (2.5 km radius), and 10 km (5 km radius) for all stacked events. For reference, we have forward modeled the slab depth model (blue line) of McCrory et al. (2012) and extrapolated a slab Moho surface (red line) assuming a 7-km-thick oceanic crust. The positive arrival we interpret as the continental Moho is shown with a green line based on the 10-km stacking distance window results. (d) Tremor density (Wech & Creager, 2008) identified through April 2018 (Wech, 2010) collapsed and projected from 5 km north and south of our line (44.428°N). The blue background shading highlights the qualitative strength of the negative arrival associated with the top of the subducting plate. The green background shading highlights the possible location of a hydrated mantle wedge based on qualitative strength of the negative arrival associated with the top of the subducting plate. The lighter blue and green colors represent a qualitatively determined weaker arrival.

Audet & Schaeffer, 2018; Hansen et al., 2012) to better constrain the depths and Vp/Vs ratios above select interfaces in subduction zone settings, it is not yet clear if our preprocessing method preserves those multiples as clearly as seen in previous broadband deployments. Future work will focus on extracting more information using the multiples with this data set as well as other nodal data sets (Wu et al., 2017). Nevertheless, we include in Figures S9, S11b, and S12b where multiples from the primary arrivals we focus on here can be observed. Thus, with the dense station spacing and relatively clear primary arrivals seen in
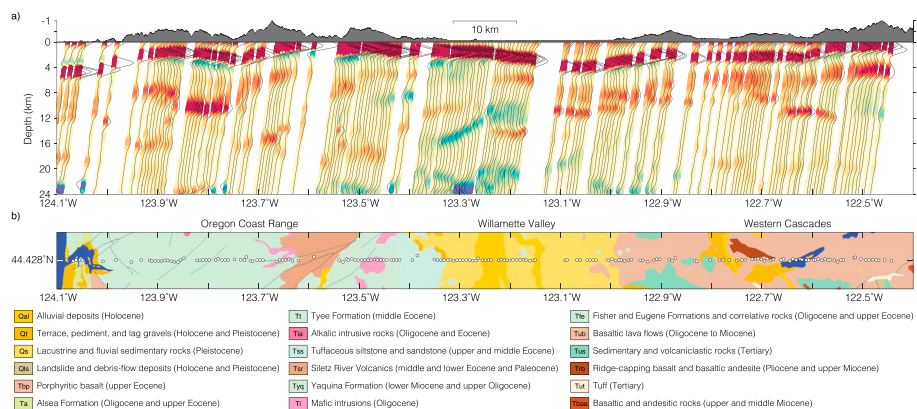

Figure 3. (a) Stacked and depth migrated radial receiver functions with a Gaussian value of 10 (~4.8 Hz) for a stacking distance window of 10 km (5 km radius) for all stacked events (no vertical exaggeration below sea level). (b) Simplified geologic map, unit descriptions, and faults (black lines) from https://gis.dogami.oregon.gov/maps/geologicmap/ (last accessed 12 April 2018). Note that the Willamette Valley is a tectonic forearc basin and indicated with mostly yellow colors in the geologic map.

our results, there is complementary benefit to deploying both nodes and broadband instruments in a hybrid deployment. We also limit our discussion to the radial RFs as our short-duration deployment yielded a narrow range of event back azimuths. However, we have included in the supporting information a figure (Figure S10) that show the transverse RFs.

3.1. Plate Tectonic-Scale Results

Stacked radial RF results (Figure 2) with a Gaussian value of 5 (~2.4 Hz) show a dipping positive arrival that is consistent with the expected arrival time of the slab Moho from the coast to ~122.9°W under the WC. For reference, we forward modeled (Zhu & Kanamori, 2000) the slab depth model of McCrory et al. (2012) using a simple 1-D velocity model (V_P = 7.0 km/s; V_s = 4.0 km/s) and extrapolated a slab Moho surface assuming a 7-km-thick oceanic crust (blue and red lines in Figure 2). The eastern edge of the slab Moho we image is remarkably consistent with previous broadband studies; however, our results show a laterally continuous feature. Conversely, the dipping negative arrival just above the slab Moho is consistent with the slab depth model (McCrory et al., 2012) and the results from previous broadband studies; however, in detail the feature we image is segmented (discontinuous) from the coast to the WC.

The positive arrival we interpret as the continental Moho is observed at ~122.9°W under the WC and continues to the eastern limit of our array, albeit at a reduced amplitude. Over 20 stations resolve this feature, and it is clearly observed even in the noisier individual station results (Figure 2a). However, previous studies have not imaged the continental Moho as far west under this section of the WC as in our results so a direct comparison with other RF results is not possible. Nevertheless, the positive arrival we interpret as the continental Moho does not extend west of ~122.9°W and its absence under the WV is consistent with the presence of a hydrated mantle wedge postulated in several previous studies (Abers et al., 2017; Blakely et al., 2005; Bostock et al., 2002). This is because a hydrated mantle wedge would predict a lower velocity mantle wedge. Thus, in comparison to the slower velocities of the crust, the continental Moho arrival might appear as weaker, absent, or inverted depending on the degree of mantle hydration and associated velocity reduction (Bostock et al., 2002).

3.2. Shallow Crustal-Scale Results

The order of magnitude greater station density afforded by our passive source nodal array allows exploration of the shallow crust in unprecedented detail along this forearc transect. In our high-frequency (~4.8 Hz) stacked and depth-migrated radial RF results (Figure 3), several laterally continuous arrivals can be observed. Perhaps most prominent is a highly variable positive arrival observed between 1 and 5 km that extends the entire length of the array. This horizon reaches its greatest depth (~5 km) at the coast and in the eastern WV and is shallowest (~1 km) around 123.6°W. The multiples of this arrival are perhaps observable along the CR and WC but appear absent under the WV likely as a result of interference from multiple reflections within the basin.

4. Discussion

The main focus of this study was to evaluate the possibility of using a dense nodal geophone array to conduct a RF analysis on a lithospheric scale, and a key metric of success would be the ability to image similar features interpreted from previous broadband RF studies across the area (e.g., Audet et al., 2010; Tauzin et al., 2017). These features include the top of the subducting Juan de Fuca Plate, the slab Moho, a hydrated mantle wedge (where continental Moho and slab conversions are absent or weak), and the continental Moho. We left our plate tectonic-scale results in the time domain (i.e., not depth migrated) for two different Gaussian filters (~0.5 and ~2.4 Hz) to facilitate this comparison (Figures S11 and S12). Within the depth estimate uncertainties of the top-of-slab (McCrory et al., 2012) and derived slab Moho, both dipping horizons are clearly seen in the stacked results (Figure 2c). Furthermore, the positive arrival we interpret as the continental Moho (~5 s) is also within existing Moho depth estimates (~40-km depth) based on other data sets (McCrory et al., 2014).

4.1. Nature of the Plate Interface

Whereas our discussion thus far has focused on ability to recover similar features found by broadband RF studies, we now focus on the structural details only visible in our dense nodal array results. In Figure 2d, we plot tremor density (Wech & Creager, 2008) identified through April 2018 (Wech, 2010) by collapsing and projecting tremor locations from 5 km north and south of our line (44.428°N). Binning tremor 5 km north and south

of our line is somewhat arbitrary, but we note that the general trend and location of peak tremor density do not vary significantly with a larger north/south bin and that the distribution is nearly symmetric about our array axis. This is relevant to our study as previous studies have indicated tremor originates at or near the plate interface (La Rocca et al., 2009; Thomas & Bostock, 2015; Wech & Creager, 2007).

A close examination of the negative arrival (strength or absence) we interpret as the top-of-slab imaged in our results reveals an interesting correlation with tremor density for this region. Both updip and downdip of the tremor density peak under the CR (~123.7–123.4°W), we observe a negative arrival that is consistent with the expected location of the top of slab. However, this negative arrival weakens and is no longer observable where tremor density is greatest (~123.7–123.4°W), whereas the positive arrival we interpret as the slab Moho is continuous over this entire distance. The local absence of a negative top-of-slab arrival suggests that there is a fundamental difference along the plate interface compared to locations both updip and downdip of the peak tremor density (~123.7–123.4°W). This observation is somewhat inconsistent with previous studies that have associated low-velocity zones (i.e., continuous negative arrivals above the slab Moho) with elevated episodic tremor and high pore fluid pressure along other sections of subduction zones (e.g., Audet & Burgmann, 2014; Audet & Schaeffer, 2018). Furthermore, previous studies that have migrated RFs to depth from the older broadband deployment (Nábělek et al., 1993) show a continuous negative shear-wave velocity perturbation above the slab Moho along the same section we observe a discontinuous negative arrival (e.g., Bostock et al., 2002; Tauzin et al., 2017).

A possible explanation for the apparent discrepancies in the nature of the plate interface as imaged from the broadband and nodal data sets is the different source distributions and thus spatial sampling/averaging. Audet et al. (2010) present RFs binned into three different back azimuths from the original broadband deployment, and the amplitude of the primary arrival associated with the top of the subducting slab under the CR varies with back azimuth and downdip location. It is possible that when all of the broadband data from multiple source back azimuths are integrated into a 2-D profile, small-scale variations are smoothed away. Thus, our array may be imaging small-scale (~10 km) heterogeneity along the plate interface, as our results are limited to one narrow back-azimuth window (Table S1). Another possibility is that our narrow event back azimuth window is not fully capturing the effects of an anisotropic slab over the region we are imaging (Song & Kim, 2012).

Along the Cascadia Subduction Zone, tremor density gradually increases both north and south of our line and is lowest in central Oregon (Wech, 2010). Relative to the northern (Washington and Vancouver Island) and southern (northern California) sections, the Oregon forearc has more crustal faults that may extend all the way to the megathrust, potentially providing paths for vertical fluid migration and reducing pore fluid pressure along the plate interface (Wells et al., 2017). Furthermore, the mafic composition of the overriding plate (ST) may limit the amount of quartz (SiO_2) invoked at other locations to effectively seal the megathrust and preserve the low-velocity zone (Audet & Burgmann, 2014; Hyndman et al., 2015). Thus, in our nodal results (Figure 2), the correlation of peak tremor density with the weak to absent negative arrival associated with the top of the slab under the CR may simply be an artifact of trying to generalize a 10-km-wide swath of spatially variable tremor locations. Or, our results might suggest that fluid overpressure (as evidenced by a low-velocity zone) may not be essential for generating subduction zone tremor even if it promotes more abundant tremor in other areas. In either case, we suggest that a dense 3-D nodal deployment may be one component of a targeted effort to better understand the complexity of the plate interface and how it is linked to variations in seismogenic processes.

4.2. Geometry of the ST

In addition to providing an opportunity to refine our understanding of the plate interface (at least on local scales), our high-frequency (~4.8 Hz) radial RF results (Figure 3) demonstrate unprecedented potential for shallow passive source imaging over a relatively large footprint. For comparison, we have also included the unmigrated version of the high-frequency RFs in Figure S13. These results include several laterally continuous arrivals that likely have an interesting tectonic interpretation. Future work will include jointly inverting surface waves with the RF results from this study into a detailed 2-D shear-wave velocity model. Therefore, for the scope of this paper and with the expectation that the structural details will be further refined, we focus on the shallow positive arrival (~1–5 km) to illustrate the details a large footprint dense nodal array can resolve.

Several existing lines of evidence suggest that the shallow positive arrival we image represents the top (or unweathered top) of the mafic ST. For example, offshore multichannel seismic reflection and refraction surveys image a fast velocity anomaly around 3- to 4-km depth at the coast (~124.1°W) that is interpreted as the mafic ST (Tréhu et al., 1994, 2012). The positive polarity arrival we image is deepest at the coast (~5 km), slightly deeper than offshore imaging observes. One possible explanation for this apparent discrepancy is that the velocity modeled used to migrate the RFs from time to depth may not be accurate enough. Future work that incorporates surface waves into a joint shear-wave velocity inversion should be able to address that possibility. Another possible explanation is that our results are imaging the unweathered top of the ST that might be deeper onshore. This is somewhat supported by the surface geology (Figure 3b) where the ST outcrops (Siletz River Volcanics). As the ST outcrops across our array and if the positive arrival we see across the array was imaging the top of the ST, we would not expect to observe (distinguish from the initial coherence peak) any arrival at those stations as the arrival would be at 0 s. Although the positive arrival is shallowest (<1 km) under this unit (~123.6°W), we still observe the arrival suggesting that it does not directly correlate with the top of the marine basalts (ST).

Further to the east under the WV, the positive arrival dips gently to the east reaching a maximum depth ~4 km (~123.1°W) and is consistent with the WV being an eastward dipping homocline (Yeats et al., 1996). It is interesting to note the positive arrival shallows to ~2 km under the westernmost WC and continues eastward well east of the surface geology that defines the modern WV. This general basin geometry has been observed before where the seismic velocities associated with the basin sediments extend under the surface volcanics of the WC (Tréhu et al., 1994). The positive arrival extends across our entire array, and therefore, we cannot define the eastern limit of the ST. However, modeling of both aeromagnetic and Bouguer gravity anomalies suggests that the ST is present in the crust across our entire array (Blakely et al., 2005) and is therefore further supportive of our interpretation.

5. Conclusions

We deployed 174 autonomous three-component 5-Hz nodal geophones in central Oregon occupying the same location of a previous broadband deployment (Nábělek et al., 1993) with 10 times the station density. Features seen in previous studies based on the older broadband deployment are clearly seen in our results and include (1) the top of the subducting Juan de Fuca Plate, (2) the slab Moho, (3) a hydrated mantle wedge, and (4) the continental Moho. Higher frequency results reveal several shallow robust features with the top of the accreted ST imaged in unprecedented detail. The RF imaging results presented here illustrate how this deployment strategy could be scaled for detailed 3-D imaging of a subduction zone interface either in a well-studied subduction zone or for rapid characterization in a subduction zone system where less is known. We envision hybrid passive source deployments with many (Large-N) nodal geophones and a backbone of broadband seismometers and/or nodal deployments that leverage controlled source offshore seismic surveys as a transformative component of future subduction zone imaging efforts.

References

Abers, G. A., van Keken, P. E., & Hacker, B. R. (2017). The cold and relatively dry nature of mantle forearcs in subduction zones. *Nature Geoscience*, *10*(5), 333–337. https://doi.org/10.1038/ngeo2922

Audet, P., Bostock, M. G., Boyarko, D. C., Brudzinski, M. R., & Allen, R. M. (2010). Slab morphology in the Cascadia fore arc and its relation to episodic tremor and slip. *Journal of Geophysical Research*, *115*, B00A16. https://doi.org/10.1029/2008JB006053

Audet, P., & Burgmann, R. (2014). Possible control of subduction zone slow-earthquake periodicity by silica enrichment. *Nature*, *510*(7505), 389–392. https://doi.org/10.1038/nature13391

Audet, P., & Schaeffer, A. J. (2018). Fluid pressure and shear zone development over the locked to slow slip region in Cascadia. *Science Advances*, *4*, eaar2982. https://doi.org/10.1126/sciadv.aar2982

Blakely, R. J., Brocher, T. M., & Wells, R. E. (2005). Subduction-zone magnetic anomalies and implications for hydrated forearc mantle. *Geology*, *33*(6), 445–448. https://doi.org/10.1130/G21447.1

Bostock, M. G., Hyndman, R. D., Rondenay, S., & Peacock, S. M. (2002). An inverted continental Moho and serpentinization of the forearc mantle. *Nature*, *417*(6888), 536–538. https://doi.org/10.1038/417536a

Dueker, K. G., & Sheehan, A. F. (1997). Mantle discontinuity structure from midpoint stacks of converted P to S waves across the Yellowstone hotspot track. *Journal of Geophysical Research*, *102*(B4), 8313–8327. https://doi.org/10.1029/96JB03857

Hansen, R. T. J., Bostock, M. G., & Christensen, N. I. (2012). Nature of the low velocity zone in Cascadia from receiver function waveform inversion. *Earth and Planetary Science Letters*, *337-338*, 25–38. https://doi.org/10.1016/j.epsl.2012.05.031

Hyndman, R. D. (2013). Downdip landward limit of Cascadia great earthquake rupture. *Journal of Geophysical Research: Solid Earth*, *118*, 5530–5549. https://doi.org/10.1002/jgrb.50390

Hyndman, R. D., McCrory, P. A., Wech, A., Kao, H., & Ague, J. (2015). Cascadia subducting plate fluids channelled to fore-arc mantle corner: ETS and silica deposition. *Journal of Geophysical Research: Solid Earth*, *120*, 4344–4358. https://doi.org/10.1002/2015JB011920

Kirby, S. H., Engdahl, E. R., & Denlinger, R. (1996). Intermediate-depth intraslab earthquakes and arc volcanism as physical expressions of crustal and uppermost mantle metamorphism in subducting slabs. In G. E. Bebout, et al. (Eds.), *Subduction: Top to bottom*, *Geophysical Monograph Series* (Vol. 96, pp. 195–214). Washington, DC: American Geophysical Union. https://doi.org/10.1029/GM096p0195

La Rocca, M., Creager, K. C., Galluzzo, D., Malone, S., Vidale, J. E., Sweet, J. R., & Wech, A. G. (2009). Cascadia tremor located near plate interface constrained by S minus P wave times. *Science*, *323*(5914), 620–623. https://doi.org/10.1126/science.1167112

Leahy, G. M., Saltzer, R. L., & Schmedes, J. (2012). Imaging the shallow crust with teleseismic receiver functions. *Geophysical Journal International*, *191*(2), 627–636. https://doi.org/10.1111/j.1365-246X.2012.05615.x

Leonard, L. J., Currie, C. A., Mazzotti, S., & Hyndman, R. D. (2010). Rupture area and displacement of past Cascadia great earthquakes from coastal coseismic subsidence. *Geological Society of America Bulletin*, *122*(11–12), 2079–2096. https://doi.org/10.1130/B30108.1

Li, X. Q., & Nábělek, J. L. (1999). Deconvolution of teleseismic body waves for enhancing structure beneath a seismometer array. *Bulletin of the Seismological Society of America*, *89*(1), 190–201.

Ligorría, J. P., & Ammon, C. J. (1999). Iterative deconvolution and receiver-function estimation. *Seismological Society of America Bulletin*, *89*, 1395–1400.

Liu, G., Persaud, P., & Clayton, R. W. (2018). Structure of the northern Los Angeles basins revealed in teleseismic receiver functions from short-term nodal seismic arrays. *Seismological Research Letters*, *89*, 1680–1689. https://doi.org/10.1785/0220180071

McCaffrey, R., King, R. W., Payne, S. J., & Lancaster, M. (2013). Active tectonics of northwestern US inferred from GPS-derived surface velocities. *Journal of Geophysical Research: Solid Earth*, *118*, 709–723. https://doi.org/10.1029/2012JB009473

McCrory, P. A., Blair, J. L., Waldhauser, F., & Oppenheimer, D. H. (2012). Juan de Fuca slab geometry and its relation to Wadati-Benioff zone seismicity. *Journal of Geophysical Research*, *117*, B09306. https://doi.org/10.1029/2012JB009407

McCrory, P. A., Hyndman, R. D., & Blair, J. L. (2014). Relationship between the Cascadia fore-arc mantle wedge, nonvolcanic tremor, and the downdip limit of seismogenic rupture. *Geochemistry, Geophysics, Geosystems*, *15*, 1071–1095. https://doi.org/10.1002/2013GC005144

Nábělek, J., Li, X. Q., Azevedo, S., Braunmiller, J., Fabritius, A., Leitner, B., et al. (1993). A high-resolution image of the Cascadia Subduction Zone from teleseismic converted phases recorded by a broadband seismic array. *Eos Transactions American Geophysical Union*, *74*(43), 431.

Porritt, R. W., Allen, R. M., & Pollitz, F. F. (2014). Seismic imaging east of the Rocky Mountains with USArray. *Earth and Planetary Science Letters*, *402*, 16–25. https://doi.org/10.1016/j.epsl.2013.10.034

Porritt, R. W., & Miller, M. S. (2018). Updates to FuncLab, a Matlab based GUI for handling receiver functions. *Computers & Geosciences*, *111*, 260–271. https://doi.org/10.1016/j.cageo.2017.11.022

Song, T., & Kim, Y. (2012). Localized seismic anisotropy associated with long-term slow-slip events beneath southern Mexico. *Geophysical Research Letters*, *39*, L09308. https://doi.org/10.1029/2012GL051324

Syracuse, E. M., van Keken, P. E., & Abers, G. A. (2010). The global range of subduction zone thermal models. *Physics of the Earth and Planetary Interiors*, *183*(1-2), 73–90. https://doi.org/10.1016/j.pepi.2010.02.004

Tauzin, B., Reynard, B., Perrillat, J., Debayle, E., & Bodin, T. (2017). Deep crustal fracture zones control fluid escape and the seismic cycle in the Cascadia Subduction Zone. *Earth and Planetary Science Letters*, *460*, 1–11. https://doi.org/10.1016/j.epsl.2016.12.007

Thomas, A. M., & Bostock, M. G. (2015). Identifying low-frequency earthquakes in central Cascadia using cross-station correlation. *Tectonophysics*, *658*, 111–116. https://doi.org/10.1016/j.tecto.2015.07.013

Tréhu, A. M., Asudeh, I., Brocher, T. M., Luetgert, J. H., Mooney, W. D., Nabelek, J. L., & Nakamura, Y. (1994). Crustal architecture of the Cascadia forearc. *Science*, *266*(5183), 237–243. https://doi.org/10.1126/science.266.5183.237

Tréhu, A. M., Blakely, R. J., & Williams, M. C. (2012). Subducted seamounts and recent earthquakes beneath the central Cascadia forearc. *Geology*, *40*(2), 103–106. https://doi.org/10.1130/G32460.1

Wang, P., Engelhart, S. E., Wang, K., Hawkes, A. D., Horton, B. P., Nelson, A. R., & Witter, R. C. (2013). Heterogeneous rupture in the great Cascadia earthquake of 1700 inferred from coastal subsidence estimates. *Journal of Geophysical Research: Solid Earth*, *118*, 2460–2473. https://doi.org/10.1002/jgrb.50101

Ward, K. M., & Lin, F. (2017). On the variability of using autonomous three-component geophones for calculate teleseismic Ps receiver functions with an application to Old Faithful, Yellowstone. *Seismological Research Letters*, *88*, 1268–1278. https://doi.org/10.1785/0220170051

Ward, K. M., Lin, F., Kiser, E. D., Thomas, A. M., & Schmandt, B., (2017). Central Oregon Dense 3C Node Transect: International Federation of Digital Seismograph Networks, Other/Seismic Network. https://doi.org/10.7914/SN/ZO_2017

Wech, A. G. (2010). Interactive tremor monitoring. *Seismological Research Letters*, *81*(4), 664–669. https://doi.org/10.1785/gssrl.81.4.664

Wech, A. G., & Creager, K. C. (2007). Cascadia tremor polarization evidence for plate interface slip. *Geophysical Research Letters*, *34*, L22306. https://doi.org/10.1029/2007GL031167

Wech, A. G., & Creager, K. C. (2008). Automatic detection and location of Cascadia tremor. *Geophysical Research Letters*, *35*, L20302. https://doi.org/10.1029/2008GL035458

Wells, R. E., Blakely, R. J., Wech, A. G., McCrory, P. A., & Michael, A. (2017). Cascadia subduction tremor muted by crustal faults. *Geology*, *45*(6), 515–518. https://doi.org/10.1130/G38835.1

Wells, R. E., Bukrey, D., Friedman, R., Pyle, D., Duncan, R. A., Haeussler, P., & Wooden, J. (2014). Geologic history of Siletzia, a large igneous province in the Oregon and Washington coast range: Correlation to the geomagnetic polarity time scale and implications for a long-lived Yellowstone hotspot. *Geosphere*, *10*(4), 692–719. https://doi.org/10.1130/GES01018.1

Wessel, P., Smith, W. H. F., Scharroo, R., Luis, J. F., & Wobbe, F. (2013). Generic Mapping Tools: Improved version released. *Eos, Transactions American Geophysical Union*, *94*(45), 409–410. https://doi.org/10.1002/2013EO450001

Wu, S., Ward, K. M., Lin, F., Farrell, J., Karplus, M., & Smith, R. B. (2017). Anatomy of Old Faithful from subsurface seismic imaging of the Yellowstone Upper Geyser Basin. *Geophysical Research Letters*, *44*, 10,240–10,247. https://doi.org/10.1002/2017GL075255

Yeats, R. S., Graven, E. P., Werner, K. S., Goldfinger, C., & Popowski, T. A. (1996). Tectonics of the Willamette Valley, Oregon. In A. M. Rogers, et al. (Eds.), *Assessing earthquake hazards and reducing risk in the Pacific Northwest*, *U.S. Geological Survey Professional Paper* (Vol. 1560, pp. 183–222).

Zhu, L., & Kanamori, H. (2000). Moho depth variation in Southern California from teleseismic receiver functions. *Journal of Geophysical Research*, *105*(B2), 2969–2980. https://doi.org/10.1029/1999JB900322